

A New Parametric Description for Line Structures in 3D Medical Images by Means of a Weighted Integral Method

Hidetoshi Goto, Takumi Naito and Hidekata Hontani

Dept. of Computer Science and Engineering, Nagoya Institute of Technology, Nagoya, Aichi, 466-8555 Japan

Keywords: Line Structure Description, Parameter Estimation Problem, Weighted Integral Method.

Abstract: The authors propose a method that describes line structures in given 3D medical images by estimating the values of model parameters: A Gaussian function is employed as the model function and the values of the parameters are estimated by means of a weighted integral method, in which you can estimate the parameter values by solving a system of linear equations of parameters which are derived from differential equations that are satisfied by the Gaussian model function. Different from many other model-based methods for the description, the proposed method requires no parameter sweep and hence can estimate the parameter values efficiently. Once you estimate the parameter values, you can describe the location, the orientation and the scale of line structures in given 3D images. Experimental results with artificial 3D images and with clinical X-ray CT ones demonstrate the estimation performance of the proposed method.

1 INTRODUCTION

In this article, the authors propose a method that accurately and efficiently describes local line structures in 3D medical images. The description explicitly denotes the location, orientation, and thickness (scale) of each line structure in given 3D images and is needed for automatically detecting and analyzing anatomical vessels or tubes of patients in computer aided diagnosis systems: Global structures of curves such as the blood vessels or the bronchi are often extracted from given images through multiple stages and you describe the local line structures at the very first stage in the curve structure extraction (Papari and Petkov, 2011). For example, active contour models (Kass et al., 1988) or active shape models (Cootes et al., 1995) are often employed for extracting curve structures and they require edge detection before the models are registered. Edges are generally detected by local operators and the performance of an edge detector is often evaluated by the accuracy of the detected edges. Not only the locations but also the directions of edges should be accurately described when you employ Euler curves for describing curve structures in given images (Kimia et al., 2003; Tamrakar and Kimia, 2007). In (Engan et al., 1999), the blurring scales of edges also play a very important role for describing curve structures in images. The accurate information of the location, the orientation, and

the scale helps to group the described local line structures into the description of global ones.

One of the most major foundations for describing local line structures, especially for estimating their scales, can be found in a conventional scale-space analysis (Lindeberg, 1994; Lindeberg, 1998), which supplies a theoretical background of the scale selection in the computation of the SIFT key-points (Lowe, 1999; Lowe, 2004). In the scale-space analysis, you blur a given image by Gaussian filters with various scales and estimate the location and the scale (size) of each structure in the image by observing the change of image features with respect to the blurring scale change. Spatial image derivatives that are normalized with respect to the blurring scale are employed for the image features. A ridge detection method proposed by Lindeberg (Lindeberg, 1998), for example, estimates the location and the scale of each ridge structure based on a ridge-strength feature computed from the scale-normalized second derivatives: The method firstly blurs a given image at various scales to obtain a set of images blurred at different scales, then detects center points of ridge structures based on the first spatial derivatives and computes the ridge-strength feature at each of the detected center points. The locations and the scales of ridge structures in the given image are finally detected by extracting the detected center points at which the ridge-strength feature is locally maximum with respect to the blurring

scale change. It should be noted that the scales of the structures are estimated by detecting the local maximum of the ridge-strength feature and that the maximum points are detected by sweeping the scale-space. Not only the method (Lindeberg, 1998) but also many other methods (*e.g.* (Zhu et al., 2010; Si and Zhu, 2012)) estimate the values of the model parameters by sweeping a parameter space. This means the parameter values estimated by those methods are essentially quantized and you need to sample the parameter space more densely in order for improving the accuracy of the parameter estimation. Steerable filters (Freeman and Adelson, 1991) are also widely used for describing local line structures especially for estimating their directions. You can continuously rotate the direction of a steerable filter with varying the value of a parameter and can estimate the direction by referring to the change of the filter response with respect to the parameter value: Steerable filter-based methods also require the sweep of the parameter space. Curvelets (Starck et al., 2002; Woiselle et al., 2011), Wavelets (Chuang and Kuo, 1996), and Gabor filters (Zhu et al., 2010; Si and Zhu, 2012) are also often employed for describing curves or ridges and their representation of line features are essentially discretized. Eigen vectors of a Hessian (Sato et al., 1998) can estimate the line directions in a continuous way but additional operations are required for accurately estimating the center location of a line structure.

The proposed method, on the other hand, can estimate the location, orientation, and size of each line structure without sweeping a parameter space. Analogous to the scale-space analysis (Lindeberg, 1994; Lindeberg, 1998), the proposed method employs a Gaussian function for representing a line structure in a given image and describes the structure by estimating the values of the parameters of the Gaussian function so that the resultant Gaussian function fits to the local line structure. For the estimation, the authors employ a weighted integral method (Ando and Nara, 2009), which was developed for estimating the temporal frequencies of one-dimensional signals.

Given a signal, a weighted integral method estimates the values of the parameters of a model function by solving a linear system in the parameters, which is derived from differential equations that are satisfied by the model function. No parameter sweeping is needed and the values obtained by the method are essentially quantization-free. The contributions of this article are as follows: The weighted integral method is formulated for the analysis of 3D images for the first time and its description performance is evaluated using artificial images and medical CT ones.

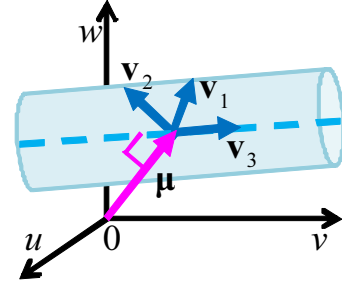


Figure 1: Parameters to be estimated for the description of a line structure.

2 WEIGHTED INTEGRAL METHOD FOR 3D IMAGES

Employing a Gaussian function, the proposed method estimates the parameters of the function for describing given local appearances by means of a weighted integral method.

2.1 Notation

Let a three-vector, $\mathbf{x} = (x, y, z)^T$, denote the coordinates in a given image and let $\Omega(\mathbf{x})$ denote a local cubic area in a given image of which center is located at \mathbf{x} . Let $\mathbf{u} = (u, v, w)$ ($-W \leq u, v, w \leq +W$) denote the local coordinates in $\Omega(\mathbf{x})$ where the origin is located at \mathbf{x} and let $I_\Omega(\mathbf{u})$ denote an image appearance in $\Omega(\mathbf{x})$.

In the proposed method, a Gaussian model function, shown in Eq. (1) is employed for describing a local image appearance.

$$f(\mathbf{u}|A, \boldsymbol{\mu}, \boldsymbol{\Sigma}) = A \exp \left\{ -\frac{1}{2}(\mathbf{u} - \boldsymbol{\mu})^T \boldsymbol{\Sigma}^{-1}(\mathbf{u} - \boldsymbol{\mu}) \right\}, \quad (1)$$

where $\boldsymbol{\mu}$ and $\boldsymbol{\Sigma}$ denote the mean vector and the covariance matrix of the Gaussian function, respectively, and a scalar, A , denotes the magnitude of the function. Let the eigenvalues of $\boldsymbol{\Sigma}$ be denoted by λ_i ($i = 1, 2, 3$) sorted in decreasing order and let the corresponding eigenvectors be denoted by \mathbf{v}_i . Let assume that a line structure is observed in $\Omega(\mathbf{x})$ and that the line structure is described by a Gaussian function. Then, $\lambda_1 \simeq \lambda_2 \gg \lambda_3 \simeq 0$ and the line direction is parallel to \mathbf{v}_3 . The location of the line structure in Ω can be described by $\boldsymbol{\mu}$ (See Fig. 1).

For the estimation of the parameters, $\boldsymbol{\mu}$ and $\boldsymbol{\Sigma}$, we rewrite $f(\cdot|\cdot)$ in (1) as follows:

$$f(\mathbf{u}|A', \boldsymbol{\theta}) = A' \exp \left\{ \sum_{\alpha, \beta, \gamma} \theta_{\alpha\beta\gamma} u^\alpha v^\beta w^\gamma \right\}. \quad (2)$$

Here, $\alpha, \beta, \gamma \in \{0, 1, 2\}$ and $1 \leq \alpha + \beta + \gamma \leq 2$. $\theta_{\alpha\beta\gamma}$ denote the coefficients of $u^\alpha v^\beta w^\gamma$ and A' denotes the magnitude. $\boldsymbol{\theta} = (\theta_{\alpha\beta\gamma})^T$ is a nine-vector. Given a local image, $I_\Omega(\mathbf{u})$, the proposed method estimates the values of the nine parameters, $\boldsymbol{\theta}$, in (2) by using a weighted integral method, of which details are described in the next subsection. It is straightforward to compute $\boldsymbol{\mu}$ and $\boldsymbol{\Sigma}$ in (1) from $\boldsymbol{\theta}$.

2.2 Weighted Integral Method

Given a signal, a weighted integral method (Ando and Nara, 2009; Goto and Hontani, 2013) estimates the values of the parameters of a model function for fitting the model to the given signal. The values are estimated not by sweeping the space of the parameters but by solving a system of linear equations of the parameters, which is derived from a set of differential equations that the model function satisfies.

The Gaussian function $f(\mathbf{u}|\cdot)$ in (2) satisfies the following differential equation at every location, \mathbf{u} :

$$\frac{\partial f(\mathbf{u}|\cdot)}{\partial u} = \sum_{\alpha,\beta,\gamma} \theta_{\alpha,\beta,\gamma} u^{\alpha-1} v^\beta w^\gamma f(\mathbf{u}|\cdot). \quad (3)$$

Let $\partial_{u^\alpha v^\beta w^\gamma} f(\mathbf{u}|\cdot)$ be denoted by $f_{u^\alpha v^\beta w^\gamma}(\mathbf{u}|\cdot)$. It should be noted that, when a local image, $I_\Omega(\mathbf{u})$, is given, the derivatives of $f_{u^\alpha v^\beta w^\gamma}(\mathbf{u}|\cdot)$ in (3) are known and the differential equation in (3) is just a linear equation of the parameters, $\theta_{\alpha\beta\gamma}$. By differentiating $f(\mathbf{u}|\cdot)$ with v and w , you obtain other linear equations of $\boldsymbol{\theta}$, and the proposed method estimates the values of $\boldsymbol{\theta}$ by solving the system of these linear equations. The values of the derivatives in these equations, though, are easily perturbed by image noises and hence the weighted integral method converts the differential equations into integral ones for estimating the parameter values more stably against the noises.

Let $c(\mathbf{u})$ denote a weight function defined on the local region, $\Omega(\mathbf{x})$. The following equation holds for any weight function because the linear equation (3) holds at every location in $\Omega(\mathbf{x})$:

$$\int_{\Omega} \left\{ f_u(\mathbf{u}) - \sum_{\alpha,\beta,\gamma} \theta_{\alpha,\beta,\gamma} u^{\alpha-1} v^\beta w^\gamma f(\mathbf{u}) \right\} c(\mathbf{u}) d\mathbf{u} = 0. \quad (4)$$

You can rewrite (4) as follows:

$$\int_{\Omega} f_u(\mathbf{u}) c(\mathbf{u}) d\mathbf{u} - \sum_{\alpha,\beta,\gamma} g^{(\alpha-1)\beta\gamma} \theta_{\alpha\beta\gamma} = 0, \quad (5)$$

where

$$g^{\alpha\beta\gamma} \equiv \int_{\Omega} u^\alpha v^\beta w^\gamma f(\mathbf{u}) c(\mathbf{u}) d\mathbf{u}. \quad (6)$$

The values of $g^{\alpha\beta\gamma}$ in (6) can be computed more stably against the noises than the values of the derivatives,

$f_{u^\alpha v^\beta w^\gamma}$, because of the spatial integration. By applying the partial integration to the first term of the left hand side of (5), you obtain the following equation:

$$\int_{\Omega} f_u(\mathbf{u}) c(\mathbf{u}) d\mathbf{u} = [f(\mathbf{u}) c(\mathbf{u})]_{\Omega} - \int_{\Omega} f(\mathbf{u}) \frac{\partial c(\mathbf{u})}{\partial u} d\mathbf{u}. \quad (7)$$

You can eliminate the first term of the right hand side of (7) if you employ a weight function such that

$$c(\mathbf{u}) = 0 \quad \text{if } \mathbf{u} \in \partial\Omega(\mathbf{x}), \quad (8)$$

where $\partial\Omega(\mathbf{x})$ denotes the boundary of the region, $\Omega(\mathbf{x})$. In the proposed method, we hence employ the Hann window function for constructing $c(\mathbf{u})$:

$$c(\mathbf{u}|\boldsymbol{\omega}) = p(u)p(v)p(w)e^{-j(\boldsymbol{\omega}^T \mathbf{u})}, \quad (9)$$

where $\boldsymbol{\omega} = (\omega_u, \omega_v, \omega_w)^T$ denotes the frequencies of the complex sinusoidal function appeared in the right hand side and $p(\cdot)$ denotes the Hann window function,

$$p(u) = \frac{1}{2} \left(1 + \cos\left(\frac{\pi u}{W}\right) \right). \quad (10)$$

The weight function (9) satisfies the condition shown in (8) and now the first term of the left hand side of (7) has an expression as follows:

$$\int_{\Omega} f_u(\mathbf{u}) c(\mathbf{u}) d\mathbf{u} = - \int_{\Omega} f(\mathbf{u}) \frac{\partial c(\mathbf{u})}{\partial u} d\mathbf{u}. \quad (11)$$

Using the expression shown in the right hand side of (11), you can compute the value of the integration more accurately because you can compute the value of $c_u(\mathbf{u})$ analytically: No finite difference approximation is needed for computing the values of the derivatives. As a result, from the weighted integral of $f_u(\mathbf{u}|\cdot)$ shown in (7), you obtain one following complex linear equation:

$$-j\omega_u g^{000} + h^u - \sum_{\alpha,\beta,\gamma} \theta_{\alpha\beta\gamma} g^{(\alpha-1)\beta\gamma} = 0, \quad (12)$$

where

$$h^u \equiv \int_{\Omega} f(\mathbf{u}) \frac{\partial p(u)}{\partial u} p(v)p(w) e^{-j(\boldsymbol{\omega}^T \mathbf{u})} d\mathbf{u}. \quad (13)$$

Analogously, using an identical weight function, you can obtain other complex equations from the derivatives, $f_v(\mathbf{u}|\cdot)$ and $f_w(\mathbf{u}|\cdot)$, such that

$$-j\omega_v g^{000} + h^v - \sum_{\alpha,\beta,\gamma} \theta_{\alpha\beta\gamma} g^{\alpha(\beta-1)\gamma} = 0, \quad (14)$$

$$-j\omega_w g^{000} + h^w - \sum_{\alpha,\beta,\gamma} \theta_{\alpha\beta\gamma} g^{\alpha\beta(\gamma-1)} = 0. \quad (15)$$

Each of the linear equations consists of two equations that correspond to the real part and the imaginary one and hence you can obtain $3 \times 2 = 6$ different linear

equations of the parameters shown in (12), (14), and (15) by computing the weighted integrals.

Having nine unknowns, you need more than nine independent linear equations for estimating the parameter values uniquely. In the experiments, four different weight functions each of which corresponds to the different frequencies, $\omega^{(k)}$ ($k = 0, 1, 2, 3$) are used for obtaining enough number of independent linear equations and the parameter values are estimated by solving the system of 24 linear equations such that

$$\begin{bmatrix} A^{(0)} \\ A^{(1)} \\ A^{(2)} \\ A^{(3)} \end{bmatrix} \boldsymbol{\theta} = \begin{bmatrix} \mathbf{b}^{(0)} \\ \mathbf{b}^{(1)} \\ \mathbf{b}^{(2)} \\ \mathbf{b}^{(3)} \end{bmatrix}, \quad (16)$$

where

$$A^{(k)} = \begin{bmatrix} g_{\mathcal{R}}^{100} & 0 & 0 & g_{\mathcal{R}}^{010} & 0 & g_{\mathcal{R}}^{001} & g_{\mathcal{R}}^{000} & 0 & 0 \\ g_I^{100} & 0 & 0 & g_I^{010} & 0 & g_I^{001} & g_I^{000} & 0 & 0 \\ 0 & g_{\mathcal{R}}^{010} & 0 & g_{\mathcal{R}}^{100} & g_{\mathcal{R}}^{001} & 0 & 0 & g_{\mathcal{R}}^{000} & 0 \\ 0 & g_I^{010} & 0 & g_I^{100} & g_I^{001} & 0 & 0 & g_I^{000} & 0 \\ 0 & 0 & g_{\mathcal{R}}^{001} & 0 & g_{\mathcal{R}}^{010} & g_{\mathcal{R}}^{100} & 0 & 0 & g_{\mathcal{R}}^{000} \\ 0 & 0 & g_I^{001} & 0 & g_I^{010} & g_I^{100} & 0 & 0 & g_I^{000} \end{bmatrix} \quad (17)$$

and

$$\mathbf{b}^{(k)} = \begin{bmatrix} -h_{\mathcal{R}}^u - \omega_u g_I^{000} \\ -h_I^u + \omega_u g_{\mathcal{R}}^{000} \\ -h_{\mathcal{R}}^v - \omega_v g_I^{000} \\ -h_I^v + \omega_v g_{\mathcal{R}}^{000} \\ -h_{\mathcal{R}}^w - \omega_w g_I^{000} \\ -h_I^w + \omega_w g_{\mathcal{R}}^{000} \end{bmatrix}. \quad (18)$$

both of which are obtained by using the weight function, $c(\mathbf{u}|\omega^{(k)})$. Here, $g_{\mathcal{R}}$ and g_I denote the real part and the imaginary part of the complex number, g .

2.3 Weight Function

As described above, different weight functions are used in the computation of $g^{\alpha\beta\gamma}$, h^u , h^v , and h^w shown in (17) and (18) in order for obtaining enough number of linear equations. Different weight functions are constructed by changing the frequencies, ω . In the experiments reported in the next section, we set

$$\omega_u^{(k)} = \frac{\pi n_u^{(k)}}{W}, \quad \omega_v^{(k)} = \frac{\pi n_v^{(k)}}{W}, \quad \omega_w^{(k)} = \frac{\pi n_w^{(k)}}{W}, \quad (19)$$

where $(n_u^{(k)}, n_v^{(k)}, n_w^{(k)}) = (+1, +1, +1), (+1, +1, -1), (+1, -1, +1), (-1, +1, +1)$ for $k = 0, 1, 2, 3$, respectively. Figure 2 shows a weight function, $c(\mathbf{u}|\omega^{(0)})$.

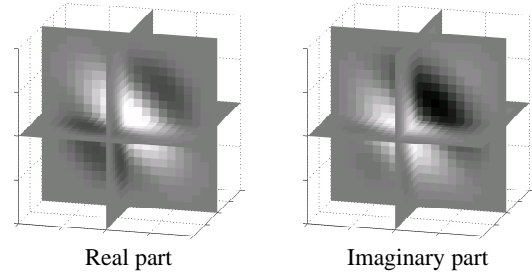


Figure 2: Profiles of the weight function, $c(\mathbf{u}|\omega^{(0)})$.

2.4 Automatic Window Size Selection

In the proposed method, the size of window, $\Omega(\mathbf{x})$, is adaptively selected at each location. As mentioned above, the coefficients of the linear systems (16) are computed by integrating the weighted appearances in Ω . Let the side length of Ω be denoted by $L (= 2W + 1)$ (see Sec. 2.1). The accuracy of the weighted integral method depends on the sizes of the windows in which the weighted appearances are integrated for computing the coefficients, $g^{\alpha\beta\gamma}$, h^u , h^v , and h^w , in the linear systems (16) (you will see details in Sec. 3.1). When the window sizes are too small, the estimation is more sensitive to measurement noises. Too large windows, on the other hand, often degrade the accuracy because neighboring structures are often included in a single window and because the resultant appearance in the window cannot be described by the model function. Hence, you need to determine an appropriate size of the window at each location in given images for making the parameter estimation more accurate. The authors propose a new method that adaptively selects the appropriate window size from a set of candidate sizes for each location in given images. As mentioned above, the weighted integral method solves the systems of linear equations with respect to the parameters. The proposed method selects a window size by evaluating the uniqueness of the solution of (16). It should be noted that, though the window sizes determined by the proposed method are quantized, the estimated values of the parameters are not quantized at all.

Let the candidates of the window sizes be denoted by $L^{(0)}, L^{(1)}, \dots, L^{(M)}$, where $M + 1$ denotes the total number of the candidates and $L^{(m-1)} < L^{(m)}$ ($m = 1, 2, \dots, M$). Let $L^{(m)} \times L^{(m)}$ window centered at \mathbf{x} be denoted by $\Omega^{(m)}(\mathbf{x})$ and let the system of the linear equations (16) obtained with $\Omega^{(m)}(\mathbf{x})$ be denoted by $A^{(m)}\boldsymbol{\theta} = \mathbf{b}^{(m)}$. The proposed method selects an appropriate window size from the set, $\{L^{(m)} | m = 0, 1, \dots, M\}$, by quantitatively evaluating the uniqueness of the solution of the linear system, $A^{(m)}\boldsymbol{\theta} = \mathbf{b}^{(m)}$. The linear system (16) can be rewritten as follows:

$$[A - \mathbf{b}]\boldsymbol{\theta}' = 0, \quad (20)$$

where $\boldsymbol{\theta}' = [\boldsymbol{\theta} \ 1]^T$. Let $A' = [A \ | \ -\mathbf{b}]$. Then, the rank of the 24×10 matrix, A' , should be equal to nine, *i.e.* $\text{rank}(A') = 9$, if (20) has a unique solution. Let the singular values of A' be denoted by $s'_1, s'_2, \dots, s'_{10}$, where $s'_n \geq s'_{n+1}$ ($n = 1, 2, \dots, 9$). We evaluate the uniqueness of the solution of (16) as follows:

$$F(A, \mathbf{b}) = \frac{s'_{10}}{s'_9}. \quad (21)$$

Note that $\text{rank}(A') = 9$ when the local appearance in Ω exactly fits the model function (1): $s'_9 > 0$ and $s'_{10} = 0$, *i.e.*, the proposed criterion, $F(\cdot, \cdot)$, is equal to zero. The proposed method, hence, judges that the local appearance in Ω is suitable for the parameter estimation when the values of F are close to zero.

At each location, \mathbf{x} , the proposed method selects the window size $L(\mathbf{x})$ that minimizes $F(A^{(m)}, \mathbf{b}^{(m)})$ for computing the coefficients of the linear equations.

$$L(\mathbf{x}) = \arg \min_{m=0,1,\dots,M} F(A^{(m)}, \mathbf{b}^{(m)}). \quad (22)$$

The candidates of the window sizes are determined as follows. Let a range of the scales that should be accurately estimated be denoted by $T_\sigma = \{\sigma \mid \sigma_{\min} \leq \sigma \leq \sigma_{\max}\}$, where σ_{\min} and σ_{\max} are the minimum scale and the maximum one to be accurately estimated, respectively. Let a range of the scale that can be accurately estimated by using the window $\Omega^{(m)}$ be denoted by $R_\sigma^{(m)}$, where $R_\sigma^{(m)} = [\alpha L^{(m)}, \beta L^{(m)}]$ and $0 < \alpha < \beta$. The candidates of the window sizes should be determined so that the following condition is satisfied:

$$T_\sigma \subseteq \bigcup_{m=0}^M R_\sigma^{(m)}. \quad (23)$$

In the proposed method, the minimum window size, $L^{(0)}$, is firstly determined so that the minimum scale is in the range $R_\sigma^{(0)}$, *i.e.*, $\alpha L^{(0)} \leq \sigma_{\min} (\leq \beta L^{(0)})$. Using the smallest window $\Omega^{(0)}$, you can accurately estimate the scales between $\alpha L^{(0)}$ and $\beta L^{(0)}$. The size of the second smallest window is then determined so that the upper boundary scale, $\beta L^{(0)}$, can be accurately estimated not only with the window $\Omega^{(0)}$ but also with $\Omega^{(1)}$, *i.e.*, $\alpha L^{(1)} \leq \beta L^{(0)}$. In the proposed method, we determine the second smallest window size so that $R_\sigma^{(1)}$ overlaps with the one quarter of $R_\sigma^{(0)}$, *i.e.* $\alpha L^{(1)} = (\alpha + 3)L^{(0)}/4$. Analogously, we determine all of the window sizes as follows:

$$L^{(m)} = \rho^m L^{(0)}, \quad (24)$$

where $\rho = (\alpha + 3)/(4\alpha)$ in the proposed method. The value of the coefficient, ρ , varies depending on the

ratio of the overlaps between $R_\sigma^{(m)}$ and $R_\sigma^{(m+1)}$. The total number of the candidates, M , is determined so that σ_{\max} can be accurately estimated using the largest window $L^{(M)}$, *i.e.* $\sigma_{\max} < \beta L^{(M)}$. Setting $m = M$, the equation (24) can be rewritten as follows:

$$\rho^M = \frac{L^{(M)}}{L^{(0)}} > \frac{\alpha \sigma_{\min}}{\beta \sigma_{\max}}. \quad (25)$$

You can determine the total number of the candidates M as follows:

$$M = \left\lceil \log_\rho \frac{L^{(M)}}{L^{(0)}} \right\rceil = \left\lceil \log_\rho \frac{\alpha \sigma_{\max}}{\beta \sigma_{\min}} \right\rceil. \quad (26)$$

For example, when $\alpha = 1/6$, $\beta = 1/4$, $\sigma_{\min} = 2.0$, $\sigma_{\max} = 20.0$, then we obtain $M = 6$. Not so many candidates are needed for covering a wide range of the scales.

3 EXPERIMENTS

3.1 Experiments with Artificial Images

Randomly sampling the parameter values of the Gaussian function, we firstly generated a set of noise-free images of a line structure and then added Gaussian noises to the images for obtaining a set of noisy ones. Applying the proposed method to the images, we evaluated the accuracy of the parameter estimation of the proposed method.

As described in Sec. 2.1, the eigenvector of the covariance matrix shown in (1) that has the minimum eigenvalue represents the direction of a target line. Let $\bar{\mathbf{v}}$ denote the true direction and let $\hat{\mathbf{v}}$ denote the direction computed from the estimated covariance matrix. For the evaluation, the window size was fixed as $W = 10$ pixel and the scale of the lines in the artificial images was set as $\bar{\sigma} = 5.0$. The direction vectors, $\bar{\mathbf{v}}$, were randomly generated under the condition that $\|\bar{\mathbf{v}}\| = 1$. Figure 3 shows some examples of the artificial images with different SN ratios. Firstly, the accuracy of the estimation the line direction was evaluated. The proposed method estimates the values of the parameters, $\theta_{\alpha, \beta, \gamma}$, and you can straightforwardly compute the line direction \mathbf{v}_3 shown in Fig. 1. Here, \mathbf{v}_3 is a unit 3-vector and can be represented by a single point on a unit sphere. Let the true direction of the line in a given image be denoted by $\hat{\mathbf{v}}$ and let the point of the unit sphere corresponding to $\hat{\mathbf{v}}$ be denoted by \hat{V} . We represented the distribution of the estimated directions, $\hat{\mathbf{v}}_3$, from the synthesized images by the points on the unit sphere and these points were projected on the tangent plane to the unit sphere at \hat{V} . The resultant distributions observed at different SN ratios are

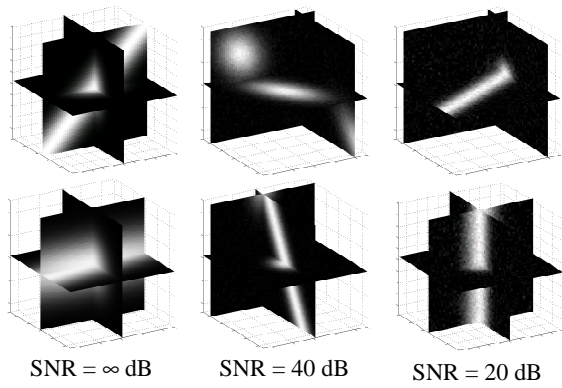


Figure 3: Examples of the artificial 3D images.

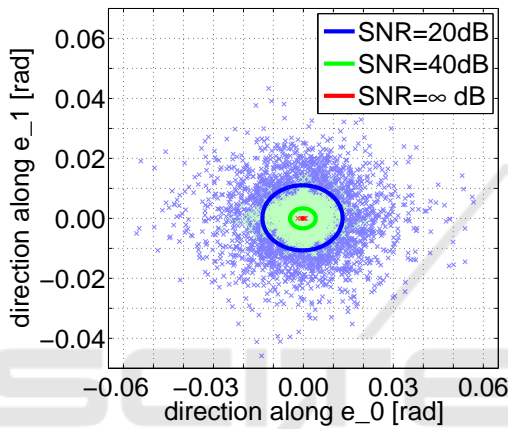


Figure 4: Experimental results of the estimation of the directions.

demonstrated in Fig. 4. The red, green and blue dots correspond to the estimated directions from the images with the SN ratio = ∞ , 40, and 20 dB, respectively. As shown in the figure, the estimation error variance increased with respect to the decrease of the SN ratio but the estimation was unbiased: The center of the dots was identical with the true direction.

Then, for evaluating the accuracy of the scale estimation, a set of the artificial images in which the line structures have varieties of the scale values was used. A graph shown in Fig. 5 shows the result. The horizontal axis of the graph indicates the values of the true scale $\bar{\sigma}$ and the vertical one indicates the ratio of the estimated scale $\hat{\sigma}$ to the true one. As shown in the graph, when the given images are noise free images, the proposed method successfully estimated the scales regardless of the value. When the SN ratio decreased, the estimation quality degraded at the smaller scales ($\bar{\sigma} < 2$) and at the larger scales ($\bar{\sigma} > 6$). It should be noted that these results were obtained with a fixed window size ($L = 2W + 1$) and that these results are useful for determining the values of α and of β , which determine the range of the scale, R_σ , in which

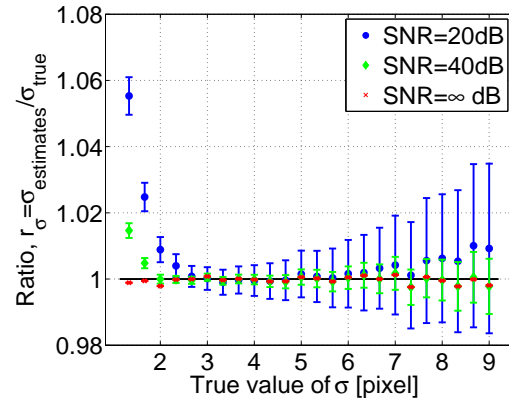


Figure 5: Experimental results of the scale estimation.

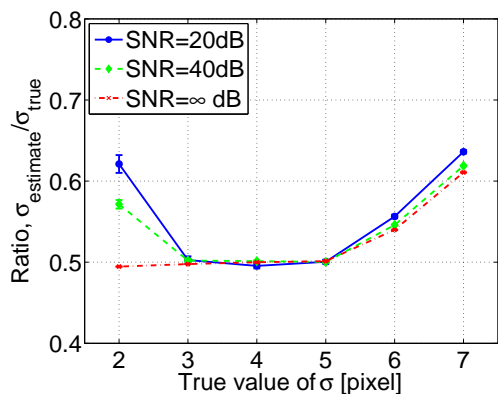
scales you can accurately estimate with the window size, L^* .

The robustness of the proposed method, the ability of the method against input images of which patterns do not strictly obey the model, is evaluated. In this article, we report on the results obtained when the input line patterns were represented by a pill-box model such that

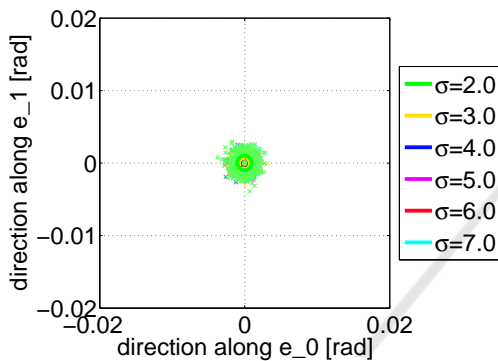
$$I(\mathbf{x}; \sigma) = \begin{cases} 1, & \text{if } x^2 + z^2 < \sigma^2, \\ 0, & \text{otherwise,} \end{cases} \quad (27)$$

The estimation performance against non-Gaussian patterns is improved by firstly blurring the input images with Gaussian of which scale is σ_0^2 , estimating the scale, $\hat{\sigma}^2$ using the propose method and outputting $\hat{\sigma}^2 = \hat{\sigma}^2 - \sigma_0^2$. Figure 6 shows the results. As shown, the proposed method unfortunately underestimated the scales, but the estimated scale values were proportional to the true ones. It should be noted that the scale space analysis (Lindeberg, 1994; Lindeberg, 1998), which is one of the most standard method for the scale estimation, is also biased: When non-Gaussian patterns are input, the scale-space analysis outputs biased scales, which are proportional to the true scales (Lindeberg, 1994). On the other hand, as shown in Fig. 6(B), the estimated directions of non-Gaussian line patterns were unbiased.

Then, we evaluated the performance of the window size selection. As mentioned above, an appropriate window size should be selected because a too large window often includes not only a target line but also neighboring other structures and fails to accurately estimate the parameter values and a too small window is too sensitive to image noises and fails to accurately estimate the parameter values. For the evaluation, we generated two sets of artificial images. One set consists of images of two separate lines with different directions and the other set consists of images of a curved line. When multiple lines are included in a



(A) Scale estimation



(B) Direction estimation

Figure 6: Experimental results obtained from a set of artificial images that satisfy the equation (27).

given image, you cannot accurately estimate the parameters and so you need to automatically select an appropriate (not too small) windows size so that the window includes only one single line structure. Top panels in Fig. 7 show some examples of the images of two lines and the bottom ones show three windows with different sizes. As shown, when the windows size is large, the two lines are included in the window. As shown in Fig. 8, when you automatically select an appropriate window size at each location in given images, you obtain more accurate estimations than when you use fixed size windows. Figure 9 shows examples in the latter set. As shown, images of curves with different curvatures are given. When a curve line is given, the image pattern in the window deviate more largely from a Gaussian straight line model as the window size is increased. As shown in Fig. 10, smaller size of windows were selected when the curvatures of the lines were larger and the estimation accuracy was improved by applying the automatic window size selection. Figure 11 shows an example of the change of $F(A, \mathbf{b})$ with respect to the window size. The left panel of Fig. 11 shows an input image and the windows with different sizes and the right panel shows the value of F computed with the three win-

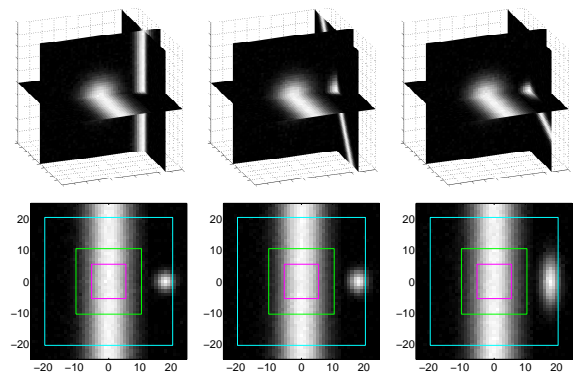


Figure 7: Examples of the two line structures. The 2D images in the bottom row show the axial-slice (x - y plane) at $z = 0$. The squares in the 2D images indicate the smallest, the middle, and the largest applied windows.

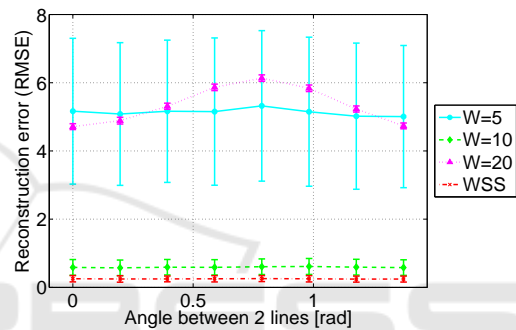


Figure 8: Experimental results of the effects of the window size selection on the estimation accuracy. In the legend, WSS means the window size selection.

dows. As shown, the value of F was the smallest when the window was enough large comparing with the line width and was enough small so that no neighboring structures was included.

3.2 Experiments with Medical Images

The authors applied the proposed method to a set of X-ray 3D medical images of the lungs for describing the structures of the blood vessels. Figure 12 shows some examples of the input images and Fig. 13 shows the descriptions obtained by the proposed method. In Fig. 13, the odd rows shows the results obtained by the proposed method and the even rows shows the surface rendering of the differences between the given images and the results. The second column, the third one, and the fourth one show the result obtained by the proposed method with the fixed window size ($W = 5, 6, 8$), respectively, and the right column shows the results obtained by the proposed method with the window size selection. In the odd rows in Fig. 13, the parameter values estimated by the proposed method are indicated by colored line segments:

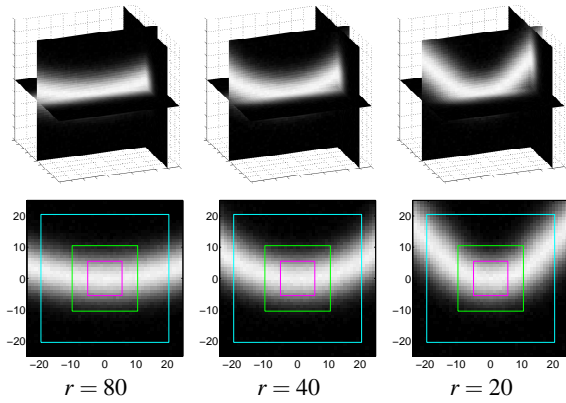


Figure 9: Examples of the curve structures. The 2D images in the bottom row show the coronal-slice (x - z plane) at $y = 0$. The squares in the 2D images indicate the smallest, the middle, and the largest applied windows.

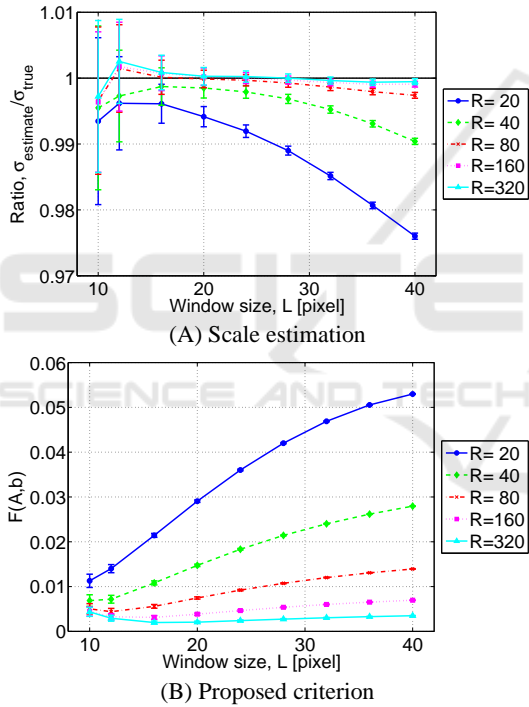


Figure 10: Experimental results of the effects of the window size selection on the estimation robustness.

The location of each segment is determined by the estimated location, $\boldsymbol{\mu}$, the direction of the segment is determined by the estimated direction, \mathbf{v}_3 , and the color of the segment is determined by the estimated scale. You can reconstruct line structures from these line segments: Generating a Gaussian that has the estimated parameters from each of the segments, you obtain line structures that have the estimated parameter values. We compared this reconstructed images with the input original ones. Let a reconstructed image be denoted by I_{re} and let the corresponding input

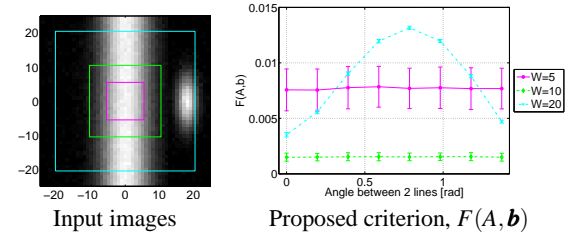


Figure 11: Experimental results of the proposed criterion, $F(A, \mathbf{b})$, obtained from the set of the artificial images of two separate lines.

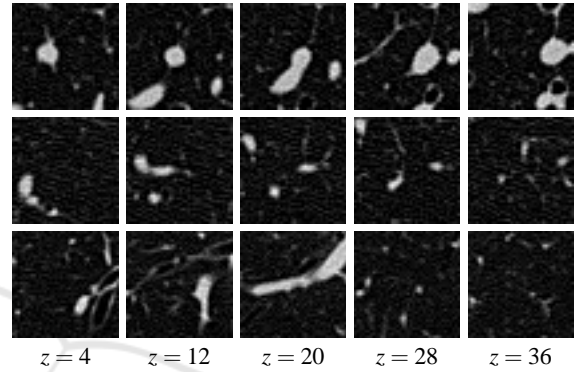


Figure 12: Examples of the X-ray CT images of lungs used in the experiments. Some axial slices are indicated.

image be denoted by I_{input} . Let $\Delta_I = I_{re} - I_{input}$. To enhance the difference, we binarized the difference image Δ_I and demonstrated binarized images in the even rows in Fig. 13. In the binarized images, blue color regions indicate $\Delta_I > 0$ and the pink regions indicate $\Delta_I < 0$. As shown in the figures, we obtained more accurate reconstruction when the window size is adaptively selected at each image location. As you can see the figures, our method failed to reconstruct the patterns of non-line structures such as junctions and we need to implement such the regions by using the line-structure descriptions. Table 1 shows the mean value of the over-detection rate and the detection failure rate for each method when the results shown in Fig. 13 were obtained. As shown, the proposed method with the window size selection can estimate the values of the parameters, that describe the line structure at each location, more accurately and more robustly than the weighted integral method with the fixed size window.

Table 1: Comparison of the mean among the results shown in Fig. 13 on the accuracy of the line description.

Proposed method	Over-detection rate	Detection failure rate
Fixed as $W = 5$	27.5 %	6.7 %
Fixed as $W = 6$	23.0 %	14.5 %
Fixed as $W = 8$	7.2 %	42.0 %
Window size selection	12.7 %	10.9 %

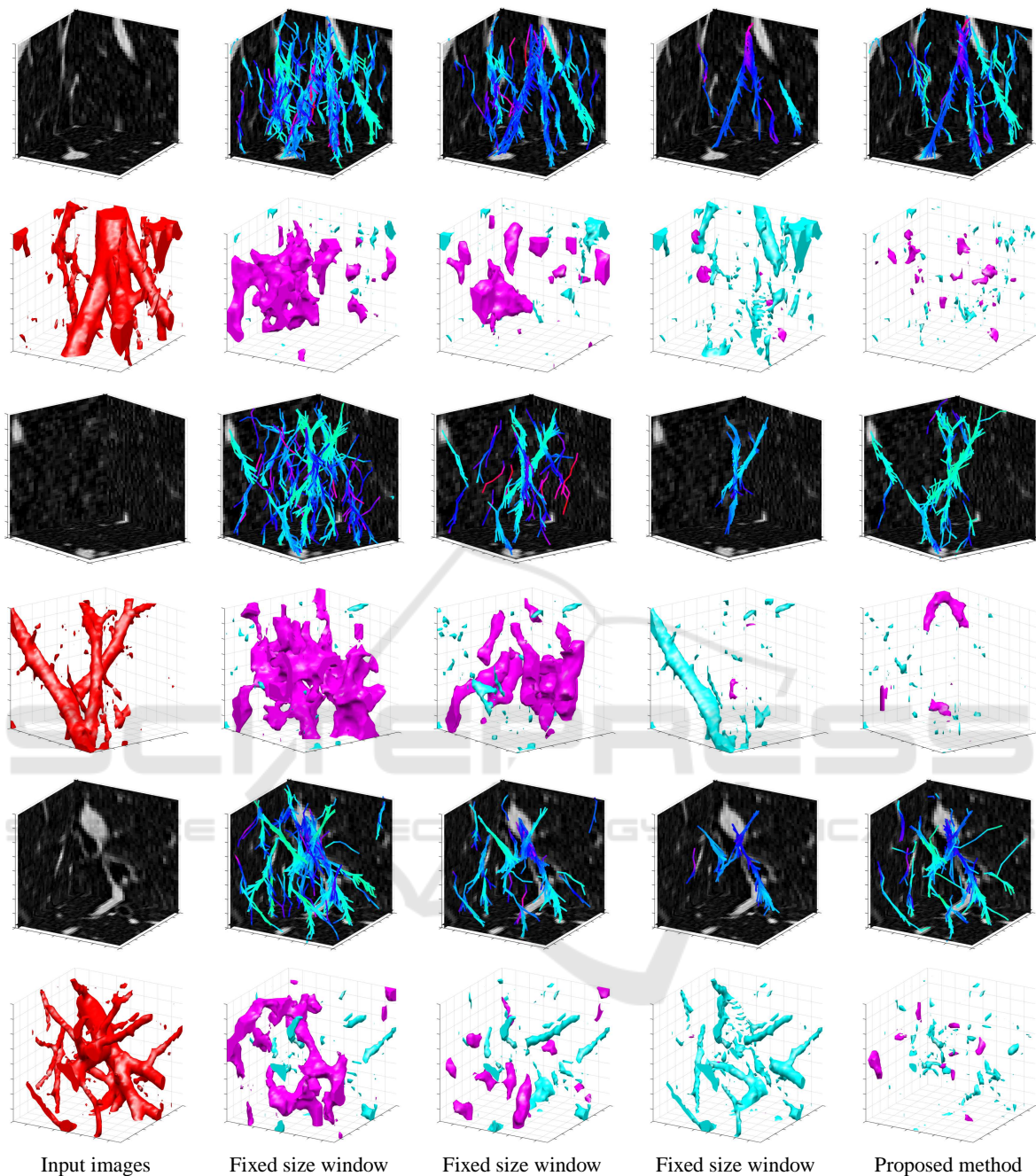


Figure 13: Examples of the descriptions obtained from the images shown in Fig. 12. The columns from second to fifth show the results by the proposed method with the fixed size window ($W = 5, 6, 8$) and the window size selection, respectively. The colors in the odd rows indicates the estimated scale, *e.g.*, cool colors indicates thin lines. In the even rows, red, blue, and pink indicate the regions of I_{input} , $\Delta_I > 0$, and $\Delta_I < 0$, respectively.

4 CONCLUSIONS

In this article, the authors proposed a new method that accurately and efficiently estimates the parameters of the Gaussian model for describing local curvi-

linear structures in 3D images. The weighted integral method linearizes the parameter estimation problem based on the differential equations satisfied by the Gaussian model function. The proposed window size selection determines appropriate window sizes by

evaluating whether a solution of the system of the linear equations exists uniquely. Experimental results demonstrated that the method estimated accurately and robustly the parameter values of local curvilinear structure in given images, and that the estimated values of parameters obtained the method describe accurately and robustly the curvilinear structures in given 3D medical images.

Future works include to develop a method that can describe local appearances using the other model functions that is not the Gaussian function, *e.g.*, the Gabor function and the wavelet, and that can automatically select an appropriate model function at each location from a set of the model function.

ACKNOWLEDGEMENTS

This work was supported by JSPS Grant-in-Aid for Scientific Research on Innovative Areas (Multidisciplinary Computational Anatomy) JSPS KAKENHI Grant Number, 26108003.

REFERENCES

- Ando, S. and Nara, T. (2009). An exact direct method of sinusoidal parameter estimation derived from finite Fourier integral of differential equation. *IEEE Trans. Signal Process.*, 57(9):3317–3329.
- Chuang, G. C.-H. and Kuo, C.-C. (1996). Wavelet descriptor of planar curves: theory and applications. *IEEE Trans. Image Process.*, 5(1):56–70.
- Cootes, T., Taylor, C., Cooper, D., and Graham, J. (1995). Active shape models – their training and application. *Comput. Vis. Image Understanding*, 61(1):38 – 59.
- Engan, K., Aase, S. O., and Håkon Husøy, J. (1999). Method of optimal directions for frame design. In *Proc., IEEE Int'l Conf. Acoustics, Speech, and Signal Process.*, volume 5, pages 2443–2446.
- Freeman, W. T. and Adelson, E. H. (1991). The design and use of steerable filters. *IEEE Trans. Pattern Anal. Mach. Intell.*, 13(9):891–906.
- Goto, H. and Hontani, H. (2013). A weighted integral method for parametrically describing local image appearance. *IPSJ Trans. Comput. Vis. Appl.*, 5:70–74.
- Kass, M., Witkin, A., and Terzopoulos, D. (1988). Snakes: Active contour models. *Int'l J. Comput. Vis.*, 1(4): 321–331.
- Kimia, B. B., Frankel, I., and Popescu, A.-M. (2003). Euler spiral for shape completion. *Int'l J. Comput. Vis.*, 54(1-3):159–182.
- Lindeberg, T. (1994). *Scale-Space Theory in Computer Vision*. Kluwer Academic Publishers.
- Lindeberg, T. (1998). Edge detection and ridge detection with automatic scale selection. *Int'l J. Comput. Vis.*, 30(2):117–156.
- Lowe, D. G. (1999). Object recognition from local scale-invariant features. In *Proc., IEEE Int'l Conf. Comput. Vis.*, volume 2, pages 1150–1157.
- Lowe, D. G. (2004). Distinctive image features from scale-invariant keypoints. *Int'l J. Comput. Vis.*, 60(2):91–110.
- Papari, G. and Petkov, N. (2011). Edge and line oriented contour detection: State of the art. *Image Vis. Computing*, 29(2-3):79 – 103.
- Sato, Y., Nakajima, S., Shiraga, N., Atsumi, H., Yoshida, S., Koller, T., Gerig, G., and Kikinis, R. (1998). Three-dimensional multi-scale line filter for segmentation and visualization of curvilinear structures in medical images. *Medical Image Anal.*, 2(2):143–168.
- Si, Z. and Zhu, S. (2012). Learning hybrid image templates (HIT) by information projection. *IEEE Trans. Pattern Anal. Mach. Intell.*, 34(7):1354–1367.
- Starck, J.-L., Candès, E. J., and Donoho, D. L. (2002). The curvelet transform for image denoising. *IEEE Trans. Image Process.*, 11(6):670–684.
- Tamrakar, A. and Kimia, B. B. (2007). No grouping left behind: From edges to curve fragments. In *IEEE Int'l Conf. Comput. Vis.*, pages 1–8.
- Woiselle, A., Starck, J.-L., and Fadili, J. (2011). 3-D data denoising and inpainting with the low-redundancy fast curvelet transform. *J. Math. Imaging Vis.*, 39(2):121–139.
- Zhu, S., Shi, K., and Si, Z. (2010). Learning explicit and implicit visual manifolds by information projection. *Pattern Recognition Letters*, 31(8):667–685.